Mon. Not. R. Astron. Soc. **379,** 297–307 (2007) doi:10.1111/j.1365-2966.2007.11967.x

CBI limits on 31 GHz excess emission in southern H II regions

C. Dickinson,[1,2⋆] R. D. Davies,[3] L. Bronfman,[4] S. Casassus,[4] R. J. Davis,[3] T. J. Pearson,[2] A. C. S. Readhead[2] and P. N. Wilkinson[3]

[1]*Jet Propulsion Laboratory, 4800 Oak Grove Drive, M/S 169-327, Pasadena, CA 91109, USA*
[2]*Chajnantor Observatory, California Institute of Technology, 1200 E. California Blvd., M/S 105-24, Pasadena, CA 91125, USA*
[3]*Jodrell Bank Observatory, University of Manchester, Macclesfield, Cheshire SK11 9DL*
[4]*Departamento de Astronomía, Universidad de Chile, Casilla 36-D, Santiago, Chile*

Accepted 2007 May 4. Received 2007 May 1; in original form 2007 February 22

ABSTRACT

We have mapped four regions of the southern Galactic plane at 31 GHz with the Cosmic Background Imager. From the maps, we have extracted the flux densities for six of the brightest H II regions in the southern sky and compared them with multifrequency data from the literature. The fitted spectral index for each source was found to be close to the theoretical value expected for optically thin free–free emission, thus confirming that the majority of flux at 31 GHz is due to free–free emission from ionized gas with an electron temperature of ≈7000–8000 K.

We also found that, for all six sources, the 31-GHz flux density was slightly higher than the predicted value from data in the literature. This excess emission could be due to spinning dust or another emission mechanism. Comparisons with 100-μm data indicate an average dust emissivity of 3.3 ± 1.7 μK $(\mathrm{MJy\,sr^{-1}})^{-1}$, or a 95 per cent confidence limit of <6.1 μK $(\mathrm{MJy\,sr^{-1}})^{-1}$. This is lower than that found in diffuse clouds at high Galactic latitudes by a factor of ∼3–4. The most significant detection (3.3σ) was found in G284.3−0.3 (RCW 49) and may account for up to ≈30 per cent of the total flux density observed at 31 GHz. Here, the dust emissivity of the excess emission is 13.6 ± 4.2 μK $(\mathrm{MJy\,sr^{-1}})^{-1}$ and is within the range observed at high Galactic latitudes.

Low-level polarized emission was observed in all six sources with polarization fractions in the range 0.3–0.6 per cent. This is likely to be mainly due to instrumental leakage and is therefore an upper limit to the free–free polarization. It corresponds to an upper limit of ∼1 per cent for the polarization of anomalous emission.

Key words: radiation mechanisms: thermal – ISM: clouds – H II regions – radio continuum: ISM.

1 INTRODUCTION

The characterization of diffuse emission from the Galaxy is important for the detailed study of fluctuations in the cosmic microwave background (CMB). Knowledge of the spectral shape and spatial morphology is important for the accurate subtraction of the foreground emission. This in turn provides a more precise view of the CMB anisotropies thus providing the most reliable cosmological information. The frequency range of greatest interest for CMB observations is ∼30–200 GHz, which is close to the minimum of foreground emission at ∼70 GHz (Bennett et al. 2003b). The diffuse Galactic foregrounds include synchrotron, free–free and vibrational (thermal) dust emissions. However, there is considerable evidence, from deep CMB data at high Galactic latitudes, for an additional component that emits in the frequency range ∼10–60 GHz (Kogut et al. 1996; Leitch et al. 1997; de Oliveira-Costa et al. 2002, 2004; Banday et al. 2003; Lagache 2003; Finkbeiner, Langston & Minter 2004; Davies et al. 2006; Fernández-Cerezo et al. 2006). The data show a strong correlation with far-infrared (FIR; ∼100 μm) emission that suggests a connection to dust grains. The most popular candidate for this anomalous component is rapidly spinning small dust grains (Draine & Lazarian 1998a,b), referred to as spinning dust. Models of spinning dust emission predict a strongly peaked spectrum at 20–40 GHz, which appears to be broadly consistent with the data. Furthermore, targeted observations of Galactic sources have shown excess emission in this frequency range (Finkbeiner et al. 2002, 2004; Casassus et al. 2004, 2006; Watson et al. 2005; Scaife et al. 2007).

At radio/microwave frequencies ($\lesssim$100 GHz), H II regions are dominated by free–free (thermal bremsstrahlung) emission from ionized gas with electron temperatures, $T_e \approx 8000$ K. The

⋆E-mail: Clive.Dickinson@jpl.nasa.gov

Table 1. Summary of CBI observations.

Object/ region	Centre RA (J2000)	Centre Dec. (J2000)	Integration[a] (h)/ noise level (Jy)	Notes
G267.9−1.1 (RCW 38)	$08^{h}58^{m}55^{s}$	$-47^{\circ}30'58''$	1.25/0.17	Contains G267.9−1.1 (RCW 38) and fainter extended components to the north (G267.8−0.9) and to the east (G268.1−1.0).
G284.3−0.3 (RCW 49)	$10^{h}24^{m}20^{s}$	$-57^{\circ}44'57''$	0.43/0.14	Low level extension to the east.
G287.4−0.6 (Carina nebula)	$10^{h}43^{m}52^{s}$	$-59^{\circ}34'33''$	2.28/0.15	Carina nebula (RCW 53, NGC 3372) covers a region $\sim 2 \times 2\,\mathrm{deg}^2$. Two bright spots: Car-I and Car-II.
G291.6−0.5 (RCW 57)	$11^{h}15^{m}00^{s}$	$-61^{\circ}16'00''$	1.15/0.18	Two distinct H II regions, G291.6−0.5 (NGC 3603) and G291.3−0.7 (NGC 3576, RCW 57)

[a]Integration times take into account data lost due to bad weather and data editing.

spectrum of free–free radiation is well understood; in the optically thin regime ($\gtrsim$1 GHz), it has a well-defined flux density spectral index[1] $\alpha \approx -0.1$ that does not vary greatly with frequency or T_e (Dickinson, Davies & Davis 2003). However, emission from spinning dust could be inherent since ion collisions with grains are expected to be the largest contributory factor in maintaining large rotational velocities required to produce significant rotational dust emission (Draine & Lazarian 1998b). Indeed, several detections are associated with H II regions (Watson et al. 2005) or planetary nebulae (PNe; Casassus et al. 2004, 2007). One previous tentative detection of spinning dust from the H II region LPH 96[201.663+1.643], which appeared to show a rising spectrum from 5 to 10 GHz, suggestive of spinning dust (Finkbeiner et al. 2002; Finkbeiner 2004), was shown to be a spurious result with only little room for spinning dust (Dickinson et al. 2006; Scaife et al. 2007).

In this paper, we have imaged several southern H II regions with the Cosmic Background Imager (CBI) to look for excess emission at 31 GHz, which could be attributed to spinning dust. These are among the brightest H II regions in the sky and are known to be dominated by free–free emission at radio frequencies up to ∼100 GHz. Furthermore, they contain copious amounts of dust within the same volume, as traced by correlated FIR (∼100 μm) emission. Using data from the literature, we model the spectrum of free–free radiation and compare the CBI data to measure or place limits on possible excess emission at 31 GHz. We also use CBI polarization data to measure and place upper limits on the polarization of free–free emission.

2 DATA

2.1 The CBI interferometer

The CBI is a 13-element interferometer, located on the high altitude site (5080-m elevation) of Chajnantor Observatory, Chile. The 0.9-m diameter Cassegrain antennas are comounted on a 6-m platform which tracks the sky on an Alt–Az mount but at a constant parallactic angle through rotation of the 'deck' platform. This gives a static u, v coverage for a given configuration and given 'deck' angle. Using the best low-noise amplifiers provide a typical system temperature $T_{sys} \sim 30$ K in a 10-GHz band centred at 31 GHz. The bandwidth is split into 10 separate 1-GHz-wide bands from 26 to 36 GHz which can be used to provide spectral information. Each antenna can measure a single left (L) or right (R) circular polarization mode, therefore, allowing observations in total intensity (LL or RR) or polarization (LR or RL). Rotation of the deck allows the 'filling' of the u, v plane to improve beam quality in Stokes I (total intensity) and combinations of LR or RL thus allowing mapping of Stokes Q and U. We use the CBI in a compact configuration that gives optimal sensitivity to extended objects and many redundant baselines. Baseline lengths range from 1 to 4 m, which correspond to angular scales ∼6 to ∼24 arcmin and a primary beam full width at half-maximum (FWHM) of 45.2 arcmin at 31 GHz.

2.2 Observations

Observations of several of the brightest southern H II regions were made with the CBI in a compact configuration during the period 2005 April–July. Here we present data for four regions: G267.9−1.1 (RCW 38), G284.3−0.3 (RCW 49), G287.4−0.6 (Carina nebula) and G291.6−0.5/G291.3−0.7 (RCW 57). These were chosen for their brightness, well-studied radio spectra and strong FIR emission that is aligned with the radio emission. Each region was observed for ∼2–3 h, at a range of deck angles to improve u, v coverage. Only short observations were required since the images are limited by dynamic range due to beam deconvolution residuals and calibration errors, that will dominate over the thermal noise for the brightest sources. Longer integrations would not significantly improve the signal-to-noise ratio, except for allowing more deck rotations. A summary of the observations is given in Table 1. The noise level was estimated from areas of the map well outside the primary beam.

2.3 Data reduction

The data were reduced and calibrated using in-house software, CBICAL, originally written for CMB data analysis (see Readhead et al. 2004a,b, and references therein for more details). The majority of data editing and flagging was done automatically, such as removing bad antennas, baselines or channels that were noisy or not working properly.

Flux calibration was achieved by observations of bright calibrator sources (primarily Jupiter) tied to the temperature of Jupiter of $T_J = 147.3 \pm 1.8$ K at 32 GHz (Readhead et al. 2004a). This, in principle, gives an accuracy of 1.3 per cent. We note that short-term gain variations and elevation corrections have not been applied due to instabilities of the noise calibration diodes in the CBI system. Checks on the data, by comparing flux densities on different nights, showed these to be below the 1 per cent level.

Ground spillover is a source of relatively strong contamination at the level of ∼0.5 Jy on the shortest baselines of the CBI. Because of

[1] Throughout the paper, the flux density spectral index, α, is defined as $S \propto \nu^{\alpha}$.

Table 2. 31 GHz integrated flux densities and derived limits on 31 GHz excess emission. Errors are quoted at the 1σ level while upper limits are given at 95 per cent ($\approx 2\sigma$) c.l. Fits were made for both a floating and fixed spectral index.

Source	Fitted S_i^{31} (Jy)	FWHM (arcmin)	Spectral index α ($S \propto \nu^{\alpha}$)	Predicted S_i^{31} (Jy)	31 GHz excess (Jy)	Excess 100-μm emissivity [μK (MJy sr^{-1})$^{-1}$]
G267.9−1.1	140.3 ± 5.1	2.6 × 2.2	−0.115 ± 0.023	140.2 ± 5.1	<14.2	<9.2
			−0.12	140.3 ± 5.1	<14.2	<9.2
G284.3−0.3	146.5 ± 5.2	7.8 × 5.6	−0.220 ± 0.074	99.6 ± 13.4	46.9 ± 14.4	13.6 ± 4.2
			−0.12	117.0 ± 5.7	29.5 ± 7.8	8.6 ± 2.3
Car-I	83.9 ± 7.6	8.8 × 6.1	−0.145 ± 0.038	79.8 ± 8.3	<24.8	<6.1
			−0.12	84.8 ± 3.8	<16.0	<5.7
Car-II	92.1 ± 8.1	9.4 × 6.9	−0.101 ± 0.048	77.5 ± 11.1	<38.1	<15.9
			−0.12	73.4 ± 3.7	18.7 ± 8.9	7.8 ± 3.7
G291.6−0.5	158.7 ± 5.8	7.1 × 7.1	−0.071 ± 0.078	143.2 ± 19.0	<50.3	<15.7
			−0.12	132.5 ± 6.6	26.2 ± 8.8	12.3 ± 4.3
G291.3−0.7[a]	88.8 ± 3.3	2.6 × 2.6	−0.161 ± 0.006	88.6 ± 0.3	<6.6	<6.7
			−0.12	85.5 ± 6.1	<15.8	<16.1

[a]For G291.3−0.7, the CBI 31-GHz data point was included when the spectral index was fitted for.
FWHM is the deconvolved size.

the comounted design, filtering based on varying fringe rates of the astronomical signal (e.g. Watson et al. 2003) cannot be used. For CMB measurements, lead/trail fields or other strategies must be employed for subtraction of ground spillover (e.g. Pearson et al. 2003). Fortunately, for very bright objects ($\gtrsim$10 Jy), the ground signal is essentially negligible. For the southern Galactic plane (longitudes ∼250–300), lead/trail fields are difficult to observe since the plane is approximately parallel to lines of constant declination, thus we have not performed the ground subtraction technique. We find that the majority of the data is unaffected by such contamination, which would be highly visible on the shortest (1 m) baselines.

2.4 Imaging and fitting

Imaging of the visibility data was carried out using the DIFMAP package employing uniform weights to give optimal resolution since we are mainly limited by dynamic range (typically 500:1 for the CBI) rather than thermal noise. The dirty images were deconvolved using the CLEAN algorithm (Högbom 1974). Primary beam corrections were applied to the CLEAN components directly so that each of the frequency channels was corrected separately with a Gaussian function of FWHM 45.2 × (ν/31 GHz) arcmin, which is a good approximation to the measured CBI primary beam (Pearson et al. 2003).

The incomplete u, v coverage of interferometric data can potentially leads to loss of flux for sources that are extended relative to the synthesized beam; ∼6 arcmin for these data. The exact amount of flux loss depends on the structure of the source and the u, v coverage. To estimate the flux loss for CBI maps presented in this paper, we simulated observations based on 100-μm *IRIS*[2] maps using the same CBI real visibilities to define the u, v coverage for each region. This is particularly important for complex extended structures. However, we found that the peak and integrated flux densities for the individual sources studied were within 5 per cent of the real values.[3] For example, G267.9−1.1, which is located in a region of extended emission, was reduced by just 3 per cent. On the other hand, the integrated flux density within a 30-arcmin radius was reduced by 58 per cent indicating that the extended emission is more strongly affected. This shows that for sources with angular diameters comparable to the synthesized beam (∼6 arcmin or smaller), the fitted flux densities are not significantly affected by the missing spatial frequencies and are correct to better than a few per cent. We therefore make no flux loss corrections for the relatively compact sources considered here. Such corrections would only increase the CBI 31-GHz flux densities quoted in Table 2.

To estimate a possible 31 GHz excess data at lower frequencies were used to make a power-law fit of the form $S = S_{31}(\nu_{\rm GHz}/31)^{\alpha}$. We used data that were believed to be reliable and did not include very low frequencies ($\lesssim$1 GHz) where the free–free emission becomes optically thick and the spectrum no longer obeys a simple power law. The best-fitting power law was then used to estimate the flux density at 31 GHz, which was compared to the observed value from the CBI. Fitted flux densities include an error term due to the fitting procedure. However, we include an additional error of 2 per cent for instabilities in fitting Gaussians when choosing different box sizes. In general, we found the fits to be relatively stable to changes in box size. Experimentation with sensible choices of boxes showed that the integrated flux densities could vary by ∼1–2 per cent. The errors quoted for the CBI fluxes therefore contain three components: an absolute calibration error (1.3 per cent), a variable fitting error and an additional 2 per cent error. This results in a typical CBI flux density error of ≈5 per cent.

3 RESULTS

3.1 G267.9−1.1 (RCW 38)

G267.9−1.1 (also known as RCW 38, Kes 5; RA (J2000) = $08^{\rm h}58^{\rm m}55^{\rm s}$, Dec. (J2000) = $-47^{\circ}30'58''$) is one of the brightest and most dense H II regions in the southern sky. The CBI 31-GHz primary-beam-corrected map is shown in Fig. 1 as contours overlaid on the *IRAS* 100-μm map. The peak 31-GHz flux density is 124.4 Jy beam^{-1} with a uniform-weighted synthesized beam FWHM of 6.0 arcmin. The dominant central component is G267.9−1.1. It has a fainter companion, G267.8−0.9 to the north and also G268.1−1.0 to the east that can be seen as extensions to

[2] Throughout the paper we use the recently reprocessed *IRAS* 100-μm map of Miville-Deschênes & Lagache (2005), '*IRIS*', which retains optimal resolution (4.3 arcmin) while removing the majority of artefacts such as striping.
[3] All fits were made using the Astronomical Image Processing Software (AIPS) task JMFIT, which provides integrated flux densities and errors for the fitted parameters.

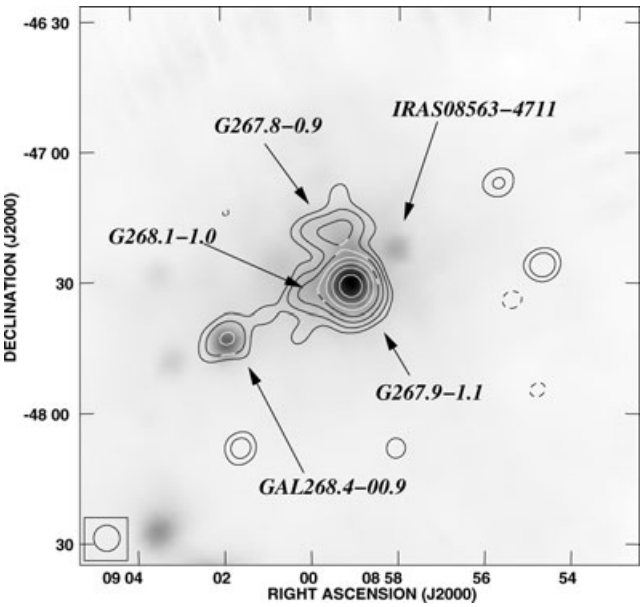

Figure 1. Map of the G267.9−1.1 (RCW 38) region. CBI 31-GHz contours are overlaid on a grey-scale image of the *IRAS* 100-μm map, with a square-root stretch. Contours are at −1 (dashed), 1, 2, 4, 8, 16, 32 and 64 per cent of the peak intensity, $S_p = 124.4$ Jy beam^{-1}. The uniform-weighted beam is 6.0×6.0 arcmin^2.

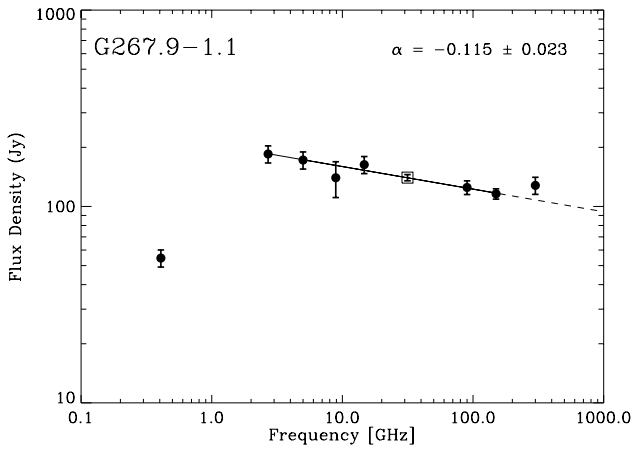

Figure 2. Spectrum of G267.9−1.1 (RCW 38). Data points (solid circles) are integrated flux densities taken from the literature (see text). Uncertainties of 10 per cent were assumed when no error was given. The CBI 31-GHz value is plotted as a square symbol. The best-fitting power law (solid line) was fitted to the data over the range 5–150 GHz and extended to higher frequencies (dashed line).

the much brighter central object.[4] The morphology is very similar to the low-frequency (0.4 and 5 GHz) maps of Shaver & Goss (1970a) and Goss & Shaver (1970).

The *IRAS* 100-μm emission is similar to that seen in the radio (Fig. 1). A compact source ≈13 arcmin to the north-west of G267.9−1.1 is visible in the 100-μm image but is not seen in the CBI or other radio maps. It is likely to be the infrared (IR) source IRAS 08563−4711 and appears to be associated with the reflection nebula BRAN 213. A relatively strong 100-μm source is visible ∼30 arcmin to the south-east of the RCW 38 region and is also detected in the CBI map, but is significantly attenuated by the 45-arcmin FWHM primary beam. This is identified as the H II region GAL 268.4−00.9 (IRAS 09002−4732).

Three Gaussian components were found to be a very good fit to the central region of the primary-beam-corrected image. However, previous data in the literature have been simply fitted with a single Gaussian (plus a baseline offset) to each source, so we have tried to replicate this Gaussian fitting procedure to make a fairer comparison. This makes a difference of ∼5–10 per cent in the integrated flux densities due to the overlapping Gaussian contributions of several closely spaced sources. The bright compact component (G267.9−1.1) contains an integrated flux density, $S_i^{31} = 140.3 \pm 5.1$ Jy with a deconvolved size of FWHM 2.6×2.2 arcmin^2. The northern component (G267.8−0.9) has $S_i \approx 19$ Jy and is $\sim 10 \times 7$ arcmin^2. A more extended Gaussian accounts for the eastern extension with $S_i \approx 39$ Jy and is $\sim 15 \times 6$ arcmin^2 but this was not included when fitting for G267.9−1.1.

The spectrum of G267.9−1.1 is plotted in Fig. 2. Data from the literature are plotted if they were believed to be reliable in relation to the fitting procedure used to determine the CBI flux densities. For example, the integrated flux densities from Very Large Array (VLA) data at 1.4 GHz could not be reliably summed due to significant flux losses which would not make a valid comparison. Similarly, the lower resolution *Wilkinson Microwave Anisotropy Probe* (*WMAP*) data (Bennett et al. 2003a) are sensitive to local extended emissions. The data points are at 0.4 and 5 GHz (Shaver & Goss 1970b), 2.7 GHz (Day, Caswell & Cooke 1972), 8.9 GHz (McGee, Newton & Batchelor 1975), 14.7 GHz (McGee & Newton 1981), 90 and 150 GHz[5] (Coble et al. 2003) and 300 GHz (Cheung et al. 1980). The free–free emission is clearly optically thick at 408 MHz and turnover at ∼1 GHz. Above 5 GHz, the emission appears to be optically thin and is best fitted by a power law over the range 5–150 GHz (omitting the CBI data point) with flux density spectral index, $\alpha = -0.115 \pm 0.023$. This agrees well with the theoretical value of $\alpha \approx -0.12$ (Dickinson et al. 2003) for $\nu \sim 30$ GHz and $T_e \approx 7500$ K (McGee et al. 1975; Caswell & Haynes 1987). From visibility–visibility correlations with the Parkes 6-cm map (Haynes, Caswell & Simons 1978), we found a consistent value of $\alpha = -0.06 \pm 0.10$. Within the CBI band (26–36 GHz), the best-fitting index was $\alpha = -0.15 \pm 0.09$, where the error was estimated assuming a 2 per cent error over the range 26–36 GHz. All the data, including the CBI data point at 31 GHz, fit extremely well with this simple free–free model, with a predicted 31-GHz flux density $S_i^{31} = 140.2 \pm 5.1$ Jy. Contributions from vibrational dust emission are only important above 200 GHz. The fitted values to G267.9−1.1 observations are summarized in Table 2. The data give an upper limit to a possible excess component of 14.2 Jy at the 95 per cent confidence level (c.l.).[6] When the spectral index was fixed at $\alpha = -0.12$, the upper limit remained at <14.2 Jy.

The FIR peak is well aligned in position with the peak in the radio. We used the *IRAS* 100-μm map to place limits on the relative dust emission. Assuming a dust emissivity of 10 μK (MJy sr^{-1})$^{-1}$ at 31 GHz, the CBI-simulated 100-μm map results in a peak flux

[4] The name G268.0−1.0 is sometimes used in the older literature and usually refers to the integrated emission from the entire region.

[5] These data were verified to be the most up-to-date measurements at this frequency (P. Mauskopf, private communication).

[6] Throughout the paper, upper limits are quoted at the 95 per cent c.l., which is $\approx 2\sigma$.

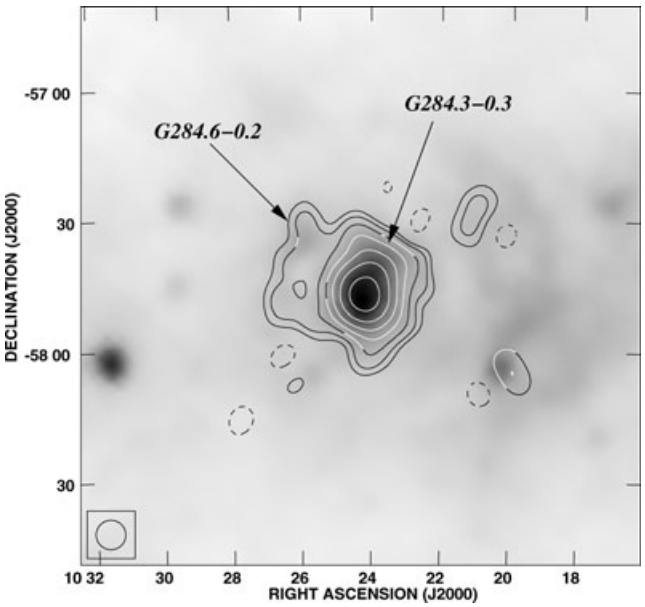

Figure 3. Map of the G284.3−0.3 (RCW 49) region. CBI 31-GHz contours are overlaid on a grey-scale image of the *IRAS* 100-μm map with a square-root stretch. Contours are at −1 (dashed), 1, 2, 4, 8, 16, 32 and 64 per cent of the peak intensity, $S_p = 79.6$ Jy beam^{-1}. The uniform-weighted beam is 6.78×6.78 arcmin^2.

density of 13.8 Jy beam^{-1} and an integrated flux density of 15.5 Jy. This corresponds to an upper limit on the dust emissivity of <9.2 μK (MJy sr^{-1})$^{-1}$; see Table 2.

3.2 G284.3−0.3 (RCW 49)

The bright H II region G284.3−0.3 (RCW 49, NGC 3247, MSH 10−54, Gum 29; RA(J2000) $=10^h\ 24^m\ 15^s$, Dec.(J2000) $= -57^\circ 46' 58''$) has a peak flux density of 79.6 Jy beam^{-1} in the 31-GHz CBI primary-beam-corrected map shown in Fig. 3. The synthesized beam has a FWHM of 6.78 arcmin. There are low-level extensions to the north and east that include the diffuse source G284.6−0.2. Wilson et al. (1970) note that the shoulder of emission to the east is probably not related to the brighter object. The CBI map agrees very well with the 5-GHz map (Goss & Shaver 1970) and the 100-μm map (Fig. 3). A single Gaussian fit to the brightest object (not including the north-east extension but allowing for a curved baseline) gave an integrated flux density of 146.5 ± 5.2 Jy with a deconvolved size of 7.8×5.6 arcmin^2. The eastern and northern extensions contain integrated flux densities of ≈25 and ≈30 Jy, respectively. However, they have negligible effect (≈1 per cent) on the fitting of the much brighter and compact component, G284.3−0.3. Stellar emission from massive O-type stars, such as those found in Westerlund 2 cluster, is negligible. The strongest emission is likely to come from colliding winds in Wolf–Rayet systems that is typically at the mJy level (Benaglia et al. 2005; Rauw et al. 2007).

The spectrum of G284.3−0.3 is plotted in Fig. 4. Data points from the literature are as for G267.9−1.1 where data are available, with the addition of 5.0 GHz (Caswell & Haynes 1987). The 5-GHz value appears to be above the line of the other data points with $S_i = 178.8$ Jy. We note that Caswell & Haynes (1987) find a flux density of 161 Jy at 5 GHz, but for a slightly smaller size of FWHM 7×5 arcmin^2, that is more consistent with the fitted spectrum. We also performed a re-analysis of the Parkes 6-cm data Haynes et al.

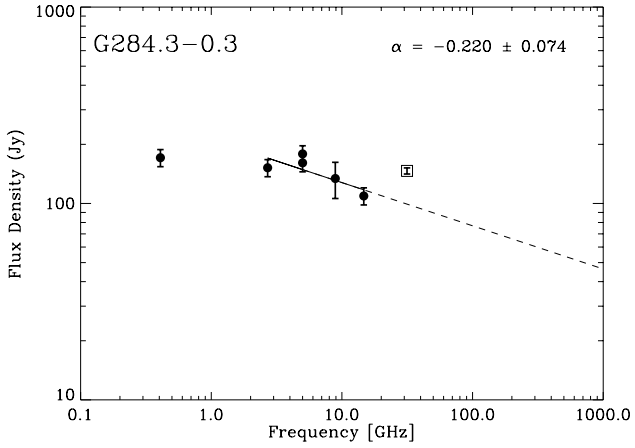

Figure 4. Spectrum of G284.3−0.3 (RCW 49). Data points (solid circles) are integrated flux densities taken from the literature (see text). Uncertainties of 10 per cent were assumed when no error was given. The CBI 31-GHz value is plotted as a square symbol. The best-fitting power law (solid line) was fitted to the data over the range 2.7–15 GHz and extended to higher frequencies (dashed line).

(1978) and find $S_i = 175$ Jy. Still, it is possible that the 14.7 GHz is a little low due to a smaller beam and smaller fitted area of 5.0×5.2 arcmin^2. A power-law fit over the range 2.7–15 GHz has a spectral index $\alpha = -0.220 \pm 0.074$, and the CBI point is well above this line; the predicted 31-GHz flux density is 99.6 ± 13.4 Jy. As can be seen from the spectrum in Fig. 4, the CBI point appears to be significantly above the expected emission from optically thin free–free alone. For this model, the excess is 46.9 ± 14.4 Jy. This is a detection of excess emission at the 3.3σ level and could account for 32 per cent of the total emission at 31 GHz. The significance increases further when fixing the spectral index to the slightly flatter value of −0.12, which is more consistent with that expected from theory for $T_e \approx 8500$ K (Azcarate 1992). For this model, the excess is 29.5 ± 7.8 Jy (3.8σ). Only when omitting the 14.7-GHz data point, the CBI point come in line with the model with a spectral index $\alpha = +0.004 \pm 0.059$.

Using only the 2.7- and 8.9-GHz data gave a spectral index of -0.11 ± 0.13, consistent with the 408-MHz data point. In this case, there still remained a significant (2.5σ) excess at 31 GHz of 29.1 ± 11.8 Jy. The spectral index within the CBI band is $\alpha = -0.11 \pm 0.09$. Cross-correlation of the simulated 5-GHz visibilities and CBI visibilities shows a very tight correlation of $P = 0.94$ with a mean slope of 0.02387 K K^{-1}, which corresponds to $\alpha = -0.05 \pm 0.10$. We therefore consider this a tentative detection of anomalous emission. Clearly, more precise data in the range 5–15 GHz are required to determine the free–free spectrum more accurately and confirm this result.

The 100-μm image is well matched to the CBI image. A simulated observation, assuming a dust emissivity of 10 μK (MJy sr^{-1})$^{-1}$ gave a flux density of 34.5 ± 1.0 Jy; the error was estimated from trying different fitting boxes. The 31 GHz excess seen in G284.3−0.3, therefore, has a 100-μm emissivity of 13.6 ± 4.2 μK (MJy sr^{-1})$^{-1}$. For a fixed spectral index, $\alpha = -0.12$, the emissivity becomes 8.6 ± 2.3 μK (MJy sr^{-1})$^{-1}$.

3.3 G287.4−0.6 (Carina nebula) region

The Carina nebula (RCW 53, NGC 3372, MSH 10−57, Gum 33, Keyhole nebula) consists of two main radio sources, Car-I

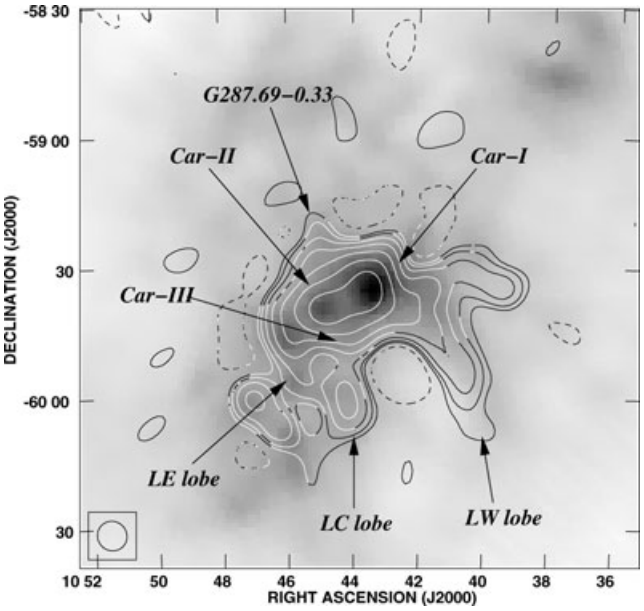

Figure 5. Map of the G287.9−1.1 (Carina nebula) region. CBI 31-GHz contours are overlaid on a grey-scale image of the *IRAS* 100-μm map with a square-root stretch. Contours are at −1 (dashed), 1, 2, 4, 8, 16, 32 and 64 per cent of the peak intensity, $S_p = 45.8\,\mathrm{Jy\,beam^{-1}}$. The uniform-weighted beam is $6.9 \times 6.7\,\mathrm{arcmin^2}$.

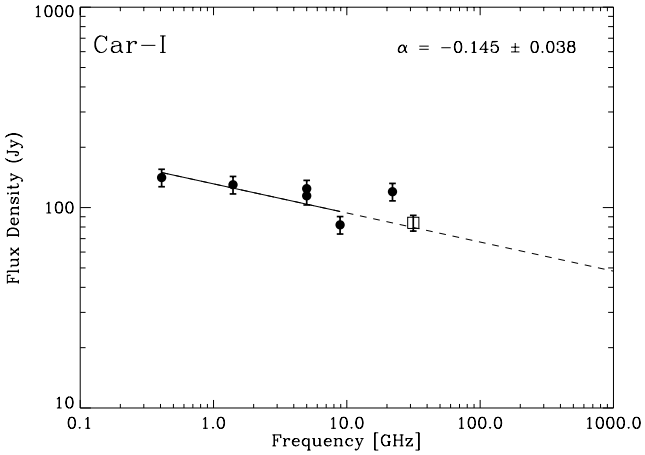

Figure 6. Spectrum of Car-I. Data points (solid circles) are integrated flux densities taken from the literature (see text). Uncertainties of 10 per cent were assumed when no error was given. The CBI 31-GHz value is plotted as a square symbol. The best-fitting power law (solid line) was fitted to the data over the range 0.4–9 GHz and extended to higher frequencies (dashed line).

(north-west) (G287.4−0.6) and Car-II (south-east) (G287.6−0.6). These are excited by the young open clusters Tr 14 and Tr 16 (Tateyama, Kaufmann & Strauss 1991) and are at a common distance of 2.2 ± 0.2 kpc. A number of weaker sources have been identified within the Carina nebula complex, which covers an area of 4 deg^2.

The CBI 31-GHz primary-beam-corrected map is shown in Fig. 5, with a synthesized beam $6.9 \times 6.7\,\mathrm{arcmin^2}$ and peak flux density, $S_p = 45.8\,\mathrm{Jy\,beam^{-1}}$. There is much extended emission in this region, particularly the several 'lobes' that extend to the south, which are also seen at lower frequencies (Whiteoak 1994; Duncan et al. 1995) and are thought to be non-thermal (Tateyama et al. 1991). The non-thermal lobes (LE, LC and LW) of Tateyama et al. (1991) are clearly seen as extensions to the south of Car-I/Car-II in Fig. 5, including Car-III (southern lobe of Car-II). The source G287.69−0.33 can be identified ∼20 arcmin to the north of Car-II with a peak flux density of ≈2 Jy. At this resolution, the brighter central region can just be resolved into the two known components, Car-I and Car-II, which are clearly seen in the 100-μm map (Fig. 5).

Two Gaussians were fitted simultaneously to the central part of the primary-beam-corrected image with a baseline slope to account for the surrounding extended emission. We found that two Gaussians could be well fitted to the data with $S_i^{31} = 83.9 \pm 7.6$ and 92.1 ± 8.1 Jy for Car-I and Car-II, respectively (Table 2). The larger errors reflect the fact that the components are slightly confused at this resolution. Their deconvolved sizes were measured to be 8.8×6.1 and $9.4 \times 6.9\,\mathrm{arcmin^2}$, respectively.

The spectrum of Car-I is shown in Fig. 6. Data points from the literature are as for G267.9−1.1 where data are available with the addition of 1.4 GHz (Retallack 1983), 8.9 GHz (Huchtmeier & Day 1975) and 22 GHz (Tateyama et al. 1991). We re-analysed the Parkes 5-GHz map of Haynes et al. (1978) and found it to be consistent with the Goss & Shaver (1970) result. In Fig. 6, we include the 22-GHz flux density from Tateyama et al. (1991) by scaling their peak flux density with their reported source size, but do not include it in the fit due to possible errors in this extrapolation. It is interesting to see the 22-GHz data point is well above the free–free model. This could be real and is consistent with spinning dust models that predict a peak at this frequency (Draine & Lazarian 1998a,b). The spectrum lies close to the optically thin free–free value down to 408 MHz (Gardner et al. 1970). The best-fitting power law over the range 0.4–9 GHz has a spectral index $\alpha = -0.145 \pm 0.038$, consistent with that predicted by theory for $T_e \approx 6600$–7400 K (Gardner et al. 1970; Caswell & Haynes 1987). The best-fitting spectral index within the CBI band is $\alpha = -0.13 \pm 0.09$. The model predicts a 31-GHz flux density $S_i^{31} = 79.8 \pm 8.3$ Jy and the CBI 31-GHz data point fits well within this model with an upper limit for an excess of 24.8 Jy (95 per cent c.l.). For a fixed spectral index, $\alpha = -0.12$, the predicted 31-GHz flux was 84.8 ± 3.8 Jy corresponding to an upper limit of < 16.0 Jy.

The CBI-simulated 100-μm map, scaled with $10\,\mu\mathrm{K}\,(\mathrm{MJy\,sr^{-1}})^{-1}$, gives a flux density of 28.0 ± 2.0 Jy for a point-like source. This translates to an upper limit on the excess dust emissivity of $<6.1\,\mu\mathrm{K}\,(\mathrm{MJy\,sr^{-1}})^{-1}$ at the 95 per cent c.l. For the fixed spectral index model, the emissivity is $<5.7\,\mu\mathrm{K}\,(\mathrm{MJy\,sr^{-1}})^{-1}$.

The spectrum of Car-II is shown in Fig. 7 with the same data plotted as for Car-I, except for omitting the 8.9-GHz value from Huchtmeier & Day (1975), which appears to be anomalously low. This is probably due to a mismatch in fitted source size and proximity of Car-I. The free–free emission remains optically thin down to 408 MHz (Gardner et al. 1970) with a spectral index $\alpha = -0.101 \pm 0.048$ fitted over the range 0.4–5 GHz, again close to the theoretical value. The predicted 31-GHz flux density is then 77.5 ± 11.1 Jy. The CBI data point lies slightly above the prediction with an upper limit of < 38.1 Jy (95 per cent c.l.) for excess emission. Although, not a statistically strong detection, it is interesting to see that the 22-GHz value is also above the free–free model alongside the 31-GHz data point. For a fixed spectral index, $\alpha = -0.12$, the predicted flux density is 73.4 ± 3.7 Jy, allowing an excess of 18.7 ± 8.9 Jy, i.e. a 2.1σ detection.

The CBI-simulated 100-μm map, scaled with $10\,\mu\mathrm{K}\,(\mathrm{MJy\,sr^{-1}})^{-1}$, gives a flux density of 24.0 ± 1.6 Jy for a point-like source. This translates to an upper limit on the excess

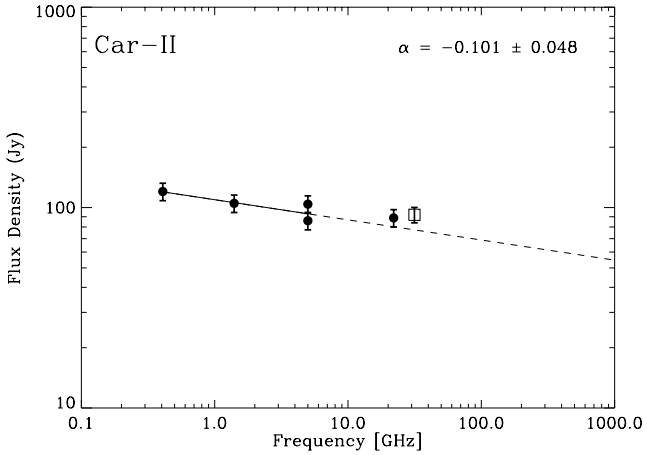

Figure 7. Spectrum of Car-II. Data points (solid circles) are integrated flux densities taken from the literature (see text). Uncertainties of 10 per cent were assumed when no error was given. The CBI 31-GHz value is plotted as a square symbol. The best-fitting power law (solid line) was fitted to the data over the range 0.4–5 GHz and extended to higher frequencies (dashed line).

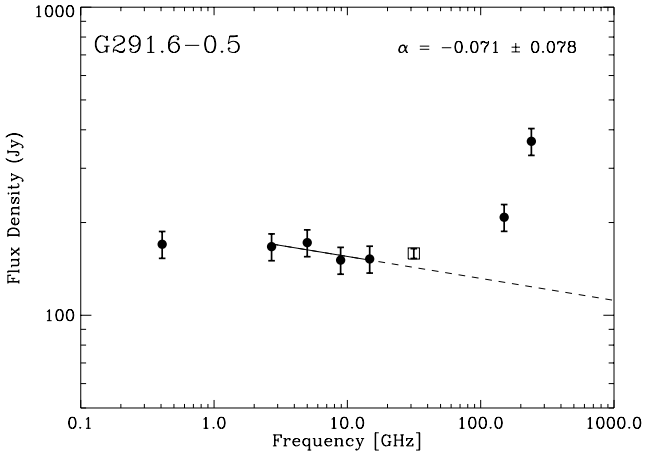

Figure 9. Spectrum of G291.6−0.5. Data points (solid circles) are integrated flux densities taken from the literature (see text). Uncertainties of 10 per cent were assumed when no error was given. The CBI 31-GHz value is plotted as a square symbol. The best-fitting power law (solid line) was fitted to the data over the range 5–15 GHz, fixing the spectral index $\alpha = -0.12$ (see text) and extended to higher frequencies (dashed line).

dust emissivity of $<15.9\,\mu$K $(\mathrm{MJy\,sr^{-1}})^{-1}$. For the fixed spectral index model, the emissivity is at $7.8 \pm 3.7\,\mu$K $(\mathrm{MJy\,sr^{-1}})^{-1}$, as summarized in Table 2.

3.4 G291.6−0.5/G291.3−0.7 (RCW 57) region

The RCW 57 region is dominated by two bright H II regions, G291.6−0.5 (NGC 3603) and G291.3−0.7 (NGC 3576), which are two of the highest luminosity optically visible H II regions in the Galaxy (Goss & Radhakrishnan 1969). The 31-GHz CBI map, with a synthesized beam FWHM of 6.7 arcmin, is shown in Fig. 8. The two H II regions dominate the map, G291.6−0.5 is the larger eastern component at the centre of the image RA(J2000) $=11^{\mathrm{h}}15^{\mathrm{m}}00^{\mathrm{s}}$, Dec.(J2000) $=-61^{\circ}16'00''$, and G291.3−0.7 is the more compact component located ≈25 arcmin to the west. The CBI 31-GHz map shows NGC 3603 as the brighter and slightly extended source with peak flux density $S_{\mathrm{p}} = 88.0\,\mathrm{Jy\,beam^{-1}}$ and NGC 3576 has $S_{\mathrm{p}} = 79.8\,\mathrm{Jy\,beam^{-1}}$ after correcting for the primary beam. The 31-GHz map agrees very well with the low-frequency GHz maps (Goss & Shaver 1970; Shaver & Goss 1970a) and the 100-μm map (Fig. 8). Some low-level extended emission is also detected in the vicinity of the dominant H II regions. A compact source to the south-east of NGC 3603 is detected and is identified as G291.9−0.7 with an integrated flux density of ≈2 Jy.

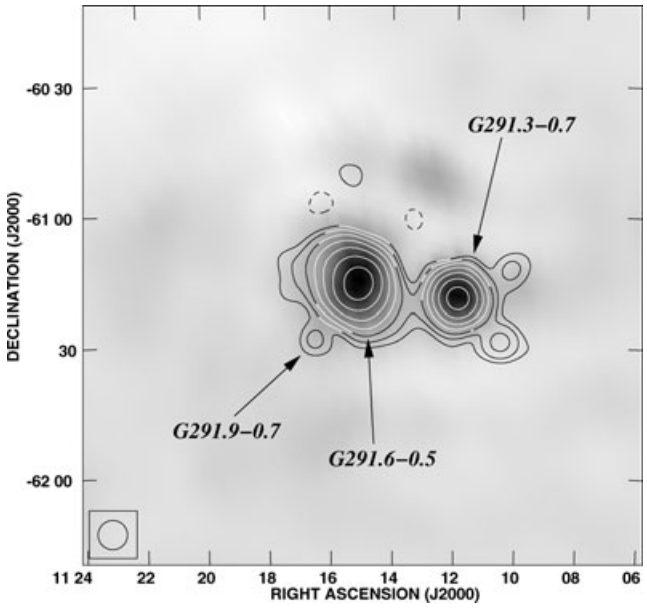

Figure 8. Map of the G291.6−0.5 (NGC 3603) and G291.7−0.3 (NGC 3576) regions. CBI 31-GHz contours are overlaid on a grey-scale image of the *IRAS* 100-μm map, with a square-root stretch. Contours are at −1 (dashed), 1, 2, 4, 8, 16, 32 and 64 per cent of the peak intensity, $S_{\mathrm{p}} = 88.0\,\mathrm{Jy\,beam^{-1}}$. The uniform-weighted beam is $6.7 \times 6.7\,\mathrm{arcmin^2}$.

Single Gaussians were fitted to the two bright sources in the CBI primary-beam-corrected map. For G291.6−0.5, we find an integrated flux density $S_{\mathrm{i}} = 158.7 \pm 5.8$ Jy with a deconvolved size $7.1 \times 7.1\,\mathrm{arcmin^2}$. The spectrum is plotted in Fig. 9. Data points from the literature are as for G267.9−1.1 where data are available, with the addition of 150- and 240-GHz data (Sabattini et al. 2005). The spectrum remains relatively flat up to a frequency of several GHz possibly indicating optically thick components. Nevertheless, we fitted a power law to data in the range 2.7–15 GHz and obtained $\alpha = -0.071 \pm 0.078$. This model gave a predicted 31-GHz flux of 143.2 ± 19.0 or an upper limit to an excess component of <50.3 Jy (95 per cent c.l.). For a fixed spectral index, $\alpha = -0.12$, the prediction becomes 132.5 ± 6.6 Jy, or an excess of 26.2 ± 8.8 Jy, i.e. a 3σ detection. The spectral index within the CBI band was found to be $\alpha = -0.12 \pm 0.09$, consistent with a typical electron temperature of $T_{\mathrm{e}} \approx$ 7000–8000 K (Wilson et al. 1970; McGee, Newton & Batchelor 1975; McGee & Newton 1981; de Pree, Nysewander & Goss 1999). The two data points at 150 and 240 GHz (Sabattini et al. 2005) provide a useful limit to the contribution of vibrational (thermal) dust emission, where they find a dust temperature $T_{\mathrm{d}} = 25.6$ K. Unless there exists a very cold dust component, the contribution from vibrational dust at 31 GHz is relatively small. Extrapolating from the Sabattini et al. values, assuming an emissivity index $\beta = +2.0$, gives a flux density of 8.9 Jy or 6 per cent of the total; this may explain the small excess observed and slightly flatter spectral index. Indeed, making a correction for the vibrational dust

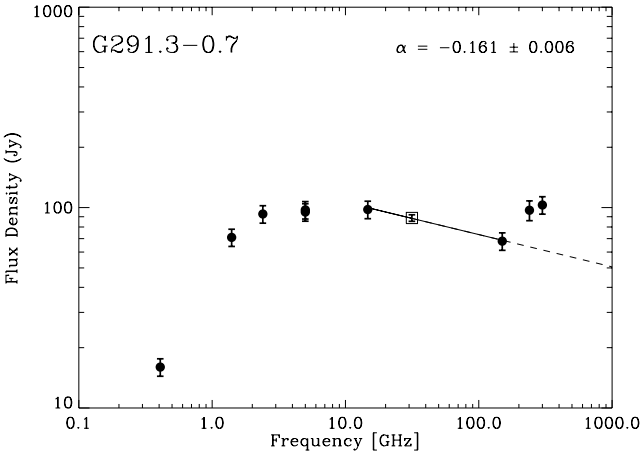

Figure 10. Spectrum of G291.3−0.7. Data points (solid circles) are integrated flux densities taken from the literature (see text). Uncertainties of 10 per cent were assumed when no error was given. The CBI 31-GHz value is plotted as a square symbol. The best-fitting power law (solid line) was fitted to the data over the range 15–150 GHz including the CBI data point (see text) and extended to higher frequencies (dashed line).

component, reduces the significance of the detection (for a fixed spectral index) to 1.2σ.

The CBI-simulated 100 μm, scaled with 10 μK (MJy sr^{-1})$^{-1}$, gives a peak brightness of 12.1 Jy beam^{-1} and an integrated flux density $S_{\rm i}^{31} = 32.1 \pm 3.0$ Jy. The 95 per cent c.l. upper limit on the excess dust emissivity is then 15.7 μK (MJy sr^{-1})$^{-1}$. For the fixed spectral index model, with no correction for a vibrational dust contribution, the emissivity is 12.3 ± 4.3 μK (MJy sr^{-1})$^{-1}$, as summarized in Table 2.

For G291.3−0.7, we find $S_{\rm i} = 88.8 \pm 3.3$ Jy with a deconvolved size 2.6×2.6 arcmin^2. The spectrum is plotted in Fig. 10 with data taken from the literature. The turnover is much more gradual indicating optically thick components and only becomes truly optically thin above ∼10 GHz. With so few data points to fit, we included the 14.7-, 150- and CBI 31-GHz data point itself in the fit. The best-fitting spectral index in the range 15–150 GHz is $\alpha = -0.161 \pm 0.006$ and is an excellent fit to the data. The upper limit is 6.7 Jy (95 per cent c.l.) for an additional component. From the data at 240 and 300 GHz, there appears to be a small contribution from vibrational dust at 150 GHz, which was found to be typically warmer ($T_{\rm d} = 31.3$ K) than for G291.6−0.5 (Sabattini et al. 2005). This is somewhat discrepant with the values found by Kuiper et al. (1987) who find warmer dust temperatures, $T_{\rm d} \approx 50$ K, based on the 60/100 μm ratios. Extrapolating from the Sabattini et al. values, for $\beta = +2.0$, gives 1.6 Jy at 31 GHz (≈2 per cent). This would steepen the spectral index further and therefore leave the possibility for a small excess at 31 GHz. However, we tried several different fits with varying assumptions (e.g. including lower frequency data), which did not allow a significant additional component at 31 GHz.

The CBI-simulated 100 μm, scaled with 10 μK (MJy sr^{-1})$^{-1}$, has a peak brightness of 5.5 Jy beam^{-1} and in integrated flux density $S_{\rm i}^{31} = 9.8 \pm 0.9$ Jy. The upper limit on the excess dust emissivity is then <6.7 μK (MJy sr^{-1})$^{-1}$ when the fit was done including the CBI data point. This will underestimate any possible excess emission since including the CBI point reduces the allowable range. However, it is such a good fit to the model, the fit is unlikely to change by much. For a fixed spectral index, $\alpha = -0.12$, the upper limit becomes 15.8 Jy (95 per cent c.l.), or a dust emissivity <16.1 μK (MJy sr^{-1})$^{-1}$. As with G291.6−0.5, the data points at 150 and 240 GHz (Sabattini et al. 2005) suggest there may be a contribution from vibrational dust emission at 31 GHz of a few Jy, or a few per cent of the total 31-GHz flux density and a much larger fraction at 150 GHz. Without more data points, and detailed modelling of the dust spectrum, it is difficult to calculate a more precise limit for this source. However, our upper limits can be considered as being conservative since these corrections are likely to steepen the free–free model allowing more room for excess emission. Nevertheless, it is clear from Fig. 10 that the CBI 31-GHz data point fits in well with the other data points following a smooth curve, leaving little or no room for possible excess emission.

Table 3. 31 GHz polarized intensity measurements. Statistically significant polarization fractions were detected in all the sources at similar level, but are likely to be contaminated by leakage terms and hence are considered upper limits (see text).

Source	$S_{\rm p}^{31}$ (mJy beam^{-1})	rms noise (mJy beam^{-1})	Polarization fraction (per cent)
G267.9−1.1	348	75	0.28 ± 0.06
G284.3−0.3	190	25	0.24 ± 0.03
Car-I	119	23	0.32 ± 0.06
Car-II	123	23	0.33 ± 0.06
G291.6−0.5	204	35	0.25 ± 0.04
G291.3−0.7	480	35	0.61 ± 0.04

3.5 Polarization limits

Stokes Q and U maps were made for each region and imaged/cleaned using the same procedure as for the total-intensity maps. Polarized intensity maps, $P = (\sqrt{Q^2 + U^2} - C)$, were made using the AIPS task COMB, where C is the correction for the Ricean noise bias, using estimates of the noise from areas of the map away from the primary beam. For all four regions, small polarized signals were detected. For both G267.9−1.1 and G284.3−0.3, a ring-like structure was observed with a peak frequency centred close to the map centre. In the Carina nebula map, we observed two point-like peaks centred on Car-I and Car-II. For G291.6−0.5 a similar faint ring-like feature is seen. The largest polarized signal, at 480 mJy beam^{-1} or 0.61 per cent polarization fraction, was observed in G291.3−0.7; a highly significant ($>10\sigma$) detection is observed in both Q and U maps. The peak polarized flux densities for all the H II regions are given in Table 3 along with the polarized fraction calculated from the ratio of peak flux densities.

Given the brightness in total intensity, the observed polarized signals are unlikely to be real since no corrections were made for instrumental leakage terms, which are expected to be at the ∼1 per cent level. The observed polarization is therefore consistent with polarization generated by the instrument itself, which is discussed further in Section 4.4.

4 DISCUSSION

4.1 Free–free emission

All the H II regions discussed in this paper are dominated by thermal free–free emission, which becomes optically thin at frequencies $\gtrsim$1 GHz. These bright sources usually consist of many compact

Table 4. Physical and observed properties. Dust temperatures are taken from Kuiper et al. (1987). The average dust temperature at high Galactic latitudes is 18.2 K (Schlegel et al. 1998). Electron temperatures were average values taken from the literature (see text for details).

Source	Radio size @31 GHz (arcmin)	FIR size @100 μm (arcmin)	T_d (K)	α ($S \propto \nu^{\alpha}$)	T_e (K)
G267.9−1.1	2.6 × 2.2	4.9 × 4.2	45	-0.115 ± 0.023	7500
G284.3−0.3	7.8 × 5.6	7.9 × 4.9	50	-0.220 ± 0.074	8500
Car-I	8.8 × 6.1	6.0 × 5.2	48	-0.145 ± 0.038	7000
Car-II	9.4 × 6.9	9.7 × 5.7	70	-0.101 ± 0.048	6600
G291.6−0.5	7.1 × 7.1	11.6 × 7.1	55	-0.071 ± 0.078	7500
G291.3−0.7	2.6 × 2.6	4.9 × 4.7	45	-0.161 ± 0.006	7500

objects that are unresolved by the CBI beam, many of which contain substantial dust which emits primarily in the FIR band (∼100 μm) within a similar volume (Table 4). At higher frequencies, the blackbody tail from the vibrating dust mechanism typically dominates and can extend down to frequencies ∼100 GHz. These two emission mechanisms largely explain the general shape of the spectrum over a wide range of frequencies from the radio to the mid-IR. Indeed, we have found that the 31-GHz flux observed with the CBI is broadly consistent with free–free emission when combined with multifrequency data taken from the literature.

The original purpose of this study was to search for evidence of spinning dust, which would show up as an additional excess component at 31 GHz, which is close to the peak of current models of spinning dust (Draine & Lazarian 1998a,b). There are inconsistencies with some of the data in the literature, where calibration errors are typically 10 per cent on quoted flux densities. In addition to this, there can be difficulties when comparing data taken at different resolutions and where different fitting techniques have been employed. Fortunately, the spectrum of free–free emission is well understood. When the radiation becomes optically thin, it has a well-defined spectral index that varies slowly with frequency and electron temperature. In fact, many authors simply fix the spectral index to the canonical radio spectral index, $\alpha = -0.1$. At higher frequencies (∼30 GHz), it steepens slightly to $\alpha = -0.14$ for $T_e = 7000$–8000 K (Dickinson et al. 2003).

We have found that the best-fitting spectral index (Table 4), not including CBI data, for all H II regions was essentially consistent with this range of values. The electron temperatures for all the H II regions are within the range ∼7000–8000 K (Table 4). Furthermore, the CBI 31-GHz data point was found to be close to the predicted flux density from a simple power-law fit to data from the literature. This confirms the dominance of free–free emission in bright H II regions. Fits were also made with a fixed spectral index, $\alpha = -0.12$, which is the mean spectral index expected for free–free emission for the range 1–30 GHz for $T_e = 8000$ K (Dickinson et al. 2003). Although, this artificially reduces the error in the model, it can help limit the impact of low or high data points that can artificially bias the spectral index, particularly when only a few data points are being fitted. For most sources, we found that the results remained stable either way.

4.2 Anomalous dust emission

We have found that at least one of the sources, G284.3−0.3 (RCW 49), shows evidence for a significant excess component, suggestive of spinning dust. Furthermore, it is compelling that all six sources are found to have a slightly higher flux density at 31 GHz than the predicted value given by a power-law model for the free–free emission. The average 100 μm dust emissivity for all the six sources is 3.3 ± 1.7 μK (MJy sr^{-1})$^{-1}$, which corresponds to a 95 per cent upper limit of 6.1 μK (MJy sr^{-1})$^{-1}$. We have discussed some possible systematics that may lead to this apparent excess, but given the conservative error bars assigned to the data, and the relative accuracy of the CBI data, this result is unlikely to be due to a systematic error. Moreover, no flux loss correction was made to the CBI data points, since it was shown to be a small correction for sources comparable to the beam size (see Section 2.4).

The most significant (3.3σ) result was for G284.3−0.3 (RCW 49). We consider this to be a tentative detection. As remarked upon in Section 3.2, there is some level of inconsistency in the lower frequency data in the range 5–14 GHz. In particular, the 5-GHz data point seems high relative to the other frequencies, yet we obtained a consistent value when we independently analysed the Parkes 6-cm map. Moreover, the 14-GHz point appears to be on the low side, while the 9-GHz value has a larger error than its neighbours. For example, taking just the 5-GHz data and the 31-GHz data alone, the spectral index is significantly flatter and is more consistent with free–free alone. Clearly more precise data in the range 5–20 GHz data are required to clarify the situation.

If spinning dust emission is found to be a significant fraction of the 31-GHz flux emission, it would be expected to originate from very small grains that can spin fast enough to produce observable emission. The smallest grains, polycyclic aromatic hydrocarbons (PAHs) are one possibility. PAHs are most readily identified as broad lines in the mid-IR spectrum that have been seen in many H II regions and PNe. The observed survival of small dust grains in hostile environments is difficult to reconcile with models (Spitzer 1978), yet strong mid-IR PAH signals are observed in active star-forming regions including RCW 49 (Churchwell et al. 2004). The spinning dust mechanism appears therefore to be still viable in such environments. It is rather surprising that the spectral index at ∼30 GHz is so similar to the canonical free–free value ($\alpha \approx -0.1$). However, the spinning dust spectrum is expected to turnover in the range ∼20–40 GHz and hence it may appear to be locally flat in this range.

4.3 Anomalous dust emissivity

The radio emission from dust in H II regions is found to be a factor of 3 to 4 less than in the cooler diffuse dust at intermediate latitudes. The limits on excess emission at 31 GHz have been converted to a dust emissivity, relative to the *IRIS* reprocessed version of the *IRAS* 100-μm map (Miville-Deschênes & Lagache 2005), which has units MJy sr^{-1}, thus our emissivities have units μK (MJy sr^{-1})$^{-1}$. We

Table 5. Comparison of 100-μm dust emissivities for H II regions and cooler dust clouds from data at or near 30 GHz. Data are the mean of the six H II regions studied in this paper, LPH 96 (Dickinson et al. 2006), average of 15 high latitude regions from *WMAP* and the all-sky *WMAP* value outside the Kp2 mask (Davies et al. 2006), LDN 1622 (Casassus et al. 2006) and G159.6−18.5 in the Perseus molecular cloud (Watson et al. 2005). Emissivities, in units μK (MJy sr^{-1})$^{-1}$, have been normalized to 31 GHz.

Source	Dust emissivity μK (MJy sr^{-1})$^{-1}$	Reference
H II regions		
Six H II regions (mean)	3.3 ± 1.7	This paper
LPH 96	5.8 ± 2.3	Dickinson et al. (2006)
Cool dust clouds		
15 regions *WMAP*	11.2 ± 1.5	Davies et al. (2006)
All-sky *WMAP*	10.9 ± 1.1	Davies et al. (2006)
LDN 1622	24.1 ± 0.7	Casassus et al. (2006)
G159.618.5	17.8 ± 0.3	Watson et al. (2005)

did this for simplicity and because it is model independent.[7] From CMB data at frequencies ∼31 GHz, and at high Galactic latitudes, the dust emissivity has a typical value of ∼10 μK (MJy sr^{-1})$^{-1}$, with variations of about a factor of ∼2 (Davies et al. 2006). We can immediately see that our tentative detection in G284.3−0.3 is consistent with the dust emissivity found at high latitude. On the other hand, the upper limits listed in Table 2 indicate that the dust emissivity is considerably lower than that found at high latitudes; the average emissivity for all six H II regions (when the spectral index was fitted for) is 3.3 ± 1.7 μK (MJy sr^{-1})$^{-1}$. In other words, if the spinning dust were to emit at the same levels as seen at in more quiescent high latitude regions of sky (at least relative to the 100-μm intensity map), we would have detected a larger excess in most of the sources studied here.

In Table 5, we have listed the 31 GHz normalized dust emissivities for H II regions and the cooler dust clouds from the literature. This emphasizes that the dust emissivity appears to be less in the H II regions than in the diffuse interstellar medium by a factor of ∼3–4, but where the average dust temperature is 18.2 K (Schlegel et al. 1998). It is also clear that the $T^{1.6}$ scaling of emissivity at high latitudes, found by Davies et al. (2006), does not hold in these regions; the warmer dust does not emit at higher levels relative to 100-μm data. This is presumably due to the different conditions in the interstellar medium, where in H II regions there is a considerably larger flux of ultraviolet (UV) photons from O–B stars that formed the ionized regions, which in turn disassociates the smaller grains required for current models of spinning dust emission.

H II regions exhibit a wide range of environmental conditions (UV radiation field, X-rays, γ-rays and electron temperatures) which affect the distribution of grain sizes and properties. The emissivity of spinning dust could then vary considerably from cloud to cloud (Davies et al. 2006). This could explain the apparent lack of anomalous emission from some regions but not others. It is also possible that some other mechanism is responsible for the bulk of the anomalous signal, including magnetodipole emission (Draine & Lazarian 1999), which strongly depends on the abundance of ferromagnetic material.

[7] Some authors have calculated dust emissivities relative other standards, including the Diffuse Infrared Background Experiment (DIRBE) 140-μm map, the Finkbeiner, Davis & Schlegel (1999) model 8 map normalized at 94 GHz or the hydrogen column density, $n_{\rm H}$, estimated from the 100-μm map of Schlegel, Finkbeiner & Davis (1998); see Finkbeiner (2004) for a useful discussion of units.

4.4 Polarization limits

The CBI polarization maps all showed some polarized emission for these sources, but at a very low level of 0.3 per cent, except for G291.3−0.7, which was at 0.6 per cent. This may be due to the fact that G291.3−0.7 is located away from the map centre by almost half a primary beam width. This could contribute extra leakage and/or errors due to the primary beam correction. We therefore take these values to be upper limits to the polarization on these angular scales. This is consistent with little or no polarization, as expected for pure free–free emission.

Free–free emission is intrinsically unpolarized, but can be polarized at the edges of H II regions by Thomson scattering. The radiation is then tangentially polarized to the edges of the cloud, at a level that depends on the viewing angle relative to the incident radiation (Rybicki & Lightman 1979). At these angular resolutions, we did not expect to see this effect since the sources are barely resolved in the CBI beam thus any secondary scattering will be averaged out by the beam. Spinning dust emission is expected to be weakly polarized at the few per cent level (Lazarian & Finkbeiner 2003). However, we did expect some level of instrumental leakage, which converts Stokes I to Stokes Q and U, at the level of ∼0.5 per cent based on earlier observations of W44 (Cartwright et al. 2005). We have not attempted to correct for leakage terms and hence it is not surprising to see such levels of polarization. This naturally explains the remarkably similar polarization fractions observed in the different H II regions. We therefore consider the quoted polarization fractions (Table 3) to be upper limits. The level of the leakage shown here is encouraging since the recent CBI polarization results (Readhead et al. 2004b; Sievers et al. 2007) had no corrections made for instrumental leakage. Given the signal-to-noise ratio of the CMB polarization detections, this level of leakage can be safely ignored, and we can be sure that the contamination is certainly below the 1 per cent level.

For the most significant detection of excess emission in G284.3−0.3, the polarization limit translates to an upper limit on the spinning dust polarization. If indeed 30 per cent of the 31 GHz emission in G284.3−0.3 is anomalous (e.g. from spinning dust), then the effective upper limit to the polarization fraction of this component is ∼1 per cent. This is lower than that observed in the Perseus cloud, G159.6−18.5, which was observed to have a polarization fraction of $3.4^{+1.5}_{-1.9}$ per cent (Battistelli et al. 2006). Such low levels of polarization are consistent with electrodipole emission from spinning grains. The slight discrepancy in polarization level may be attributed to varying levels of ferromagnetic material, which through magnetodipole emission can be much more highly polarized (Draine & Lazarian 1999).

5 CONCLUSIONS

Observations of six bright H II regions suggest a small amount of excess emission at 31 GHz, based on fitting a free–free model from data in the literature. The dominant source of emission comes from optically thin free–free emission with a spectral index $\alpha \approx -0.12$. However, we find that all the sources were slightly brighter at 31 GHz relative to the simple free–free model. The average 100 μm dust emissivity for the six H II regions was found to be 3.3 ± 1.7 μK (MJy sr^{-1})$^{-1}$, or a 95 per cent confidence limit of <6.1 μK (MJy sr^{-1})$^{-1}$. This is lower by a factor of ∼3–4 compared to cooler

diffuse clouds at high Galactic latitudes (Table 5). However, only one source, G284.3−0.3 (RCW 49), was found to be statistically significant with a 100 μm dust emissivity of 13.6 ± 4.2 μK $(\mathrm{MJy\,sr^{-1}})^{-1}$ (3.3σ). For this source, there are several caveats in interpreting and using data from the literature, which could reduce the significance of this result. New data in the range 5–30 GHz, particularly from well-calibrated instruments, are required to clarify whether our tentative detection holds. The dust emissivity, relative to the 100-μm map for this object, is consistent with that found in diffuse clouds at high Galactic latitudes (Table 5). For the majority of the other sources, only upper limits could be obtained which appear to show that the dust emissivity is in fact lower than that observed at high Galactic latitudes.

We observed very low level (0.3–0.6 per cent) polarization at 31 GHz from all the H II regions studied here. The level is consistent with that expected from instrumental leakage in the CBI instrument. This validates claims that the instrumental leakage is negligible (<1 per cent) for recent detections of CMB polarization with the CBI.

ACKNOWLEDGMENTS

CD thanks Barbara and Stanley Rawn Jr for funding a fellowship at the California Institute of Technology for part of this work. We thank the staff and engineers at the Chajnantor Observatory for their hard work and continuing support. In particular, we thank Cristobal Achermann, Ricardo Bustos, Rodrigo Reeves and Nolberto Oyarace. SC acknowledges support from FONDECYT grant 1060827. SC and LB acknowledge support from the Chilean Center for Astrophysics FONDAP 15010003. Part of the research described in this paper was carried out at the Jet Propulsion Laboratory, California Institute of Technology, under a contract with the National Aeronautics and Space Administration.

REFERENCES

Azcarate I. N., 1992, Ap&SS, 194, 225
Banday A. J., Dickinson C., Davies R. D., Davis R. J., Górski K. M., 2003, MNRAS, 345, 897
Battistelli E. S., Rebolo R., Rubiño-Martín J. A., Hildebrandt S. R., Watson R. A., Gutiérrez C., Hoyland R. J., 2006, ApJ, 645, L141
Benaglia P., Romero G. E., Koribalski B., Pollock A. M. T., 2005, A&A, 440, 743
Bennett C. L. et al., 2003a, ApJS, 148, 1
Bennett C. L. et al., 2003b, ApJS, 148, 97
Cartwright J. K., Pearson T. J., Readhead A. C. S., Shepherd M. C., Sievers J. L., Taylor G. B., 2005, ApJ, 623, 11
Casassus S., Readhead A. C. S., Pearson T. J., Nyman L.-Å, Shepherd M. C., Bronfman L., 2004, ApJ, 603, 599
Casassus S., Cabrera G. F., Förster F., Pearson T. J., Readhead A. C. S., Dickinson C., 2006, ApJ, 639, 951
Casassus S., Nyman L.-A., Dickinson C., Pearson T. J., Readhead A. C., 2007, MNRAS, submitted (arXiv:0706.0738)
Caswell J. L., Haynes R. F., 1987, A&A, 171, 261
Cheung L. H., Frogel J. A., Hauser M. G., Gezari D. Y., 1980, ApJ, 240, 74
Churchwell E. et al., 2004, ApJS, 154, 322
Coble K. et al., 2003, preprint (astro-ph/0301599)
Davies R. D., Dickinson C., Banday A. J., Jaffe T. R., Górski K. M., Davis R. J., 2006, MNRAS, 370, 1125
Day G. A., Caswell J. L., Cooke D. J., 1972, Aust. J. Phys. Astrophys. Suppl., 25, 1
de Oliveira-Costa A. et al., 2002, ApJ, 567, 363
de Oliveira-Costa A., Tegmark M., Davies R. D., Gutiérrez C. M., Lasenby A. N., Rebolo R., Watson R. A., 2004, ApJ, 606, L89
de Pree C. G., Nysewander M. C., Goss W. M., 1999, AJ, 117, 2902
Dickinson C., Davies R. D., Davis R. J., 2003, MNRAS, 341, 369
Dickinson C., Casassus S., Pineda J. L., Pearson T. J., Readhead A. C. S., Davies R. D., 2006, ApJ, 643, L111
Draine B. T., Lazarian A., 1998a, ApJ, 494, L19
Draine B. T., Lazarian A., 1998b, ApJ, 508, 157
Draine B. T., Lazarian A., 1999, ApJ, 512, 740
Duncan A. R., Stewart R. T., Haynes R. F., Jones K. L., 1995, MNRAS, 277, 36
Fernández-Cerezo S. et al., 2006, MNRAS, 370, 15
Finkbeiner D. P., 2004, ApJ, 614, 186
Finkbeiner D. P., Davis M., Schlegel D. J., 1999, ApJ, 524, 867
Finkbeiner D. P., Schlegel D. J., Curtis F., Heiles C., 2002, ApJ, 566, 898
Finkbeiner D. P., Langston G. I., Minter A. H., 2004, ApJ, 617, 350
Gardner F. F., Milne D. K., Metzger P. G., Wilson T. L., 1970, A&A, 7, 349
Goss W. M., Radhakrishnan V., 1969, Astrophys. Lett., 4, 199
Goss W. M., Shaver P. A., 1970, Aust. J. Phys. Astrophys. Suppl., 14, 1
Haynes R. F., Caswell J. L., Simons L. W. J., 1978, Aust. J. Phys. Astrophys. Suppl., 45, 1
Högbom J. A., 1974, A&A, 15, 417
Huchtmeier W. K., Day G. A., 1975, A&A, 41, 153
Kogut A., Banday A. J., Bennett C. L., Gorski K. M., Hinshaw G., Smoot G. F., Wright E. I., 1996, ApJ, 464, L5
Kuiper T. B. H., Whiteoak J. B., Fowler J. W., Rice W., 1987, MNRAS, 227, 1013
Lagache G., 2003, A&A, 405, 813
Lazarian A., Finkbeiner D., 2003, New Astron. Rev., 47, 1107
Leitch E. M., Readhead A. C. S., Pearson T. J., Myers S. T., 1997, ApJ, 486, L23
McGee R. X., Newton L. M., 1981, MNRAS, 196, 889
McGee R. X., Newton L. M., Batchelor R. A., 1975, Aust. J. Phys., 28, 185
Miville-Deschênes M.-A., Lagache G., 2005, ApJS, 157, 302
Pearson T. J. et al., 2003, ApJ, 591, 556
Rauw G., Manfroid J., Gosset E., Nazé Y., Sana H., De Becker M., Foellmi C., Moffat A. F. J., 2007, A&A, 463, 981
Readhead A. C. S. et al., 2004a, ApJ, 609, 498
Readhead A. C. S. et al., 2004b, Sci, 306, 836
Retallack D. S., 1983, MNRAS, 204, 669
Rybicki G. B., Lightman A. P., 1979, Radiative Processes in Astrophysics. Wiley, New York
Sabattini L. et al., 2005, A&A, 439, 595
Scaife A. et al., 2007, MNRAS, 377, L69
Schlegel D. J., Finkbeiner D. P., Davis M., 1998, ApJ, 500, 525
Shaver P. A., Goss W. M., 1970a, Aust. J. Phys. Astrophys. Suppl., 14, 77
Shaver P. A., Goss W. M., 1970b, Aust. J. Phys. Astrophys. Suppl., 14, 133
Sievers J. L. et al., 2007, ApJ, 660, 976
Spitzer L., 1978, Physical Processes in the Interstellar Medium. Wiley, New York
Tateyama C. E., Kaufmann P., Strauss F. M., 1991, MNRAS, 249, 716
Watson R. A. et al., 2003, MNRAS, 341, 1057
Watson R. A., Rebolo R., Rubiño-Martin J. A., Hildebrandt S., Gutièrrez C. M., Fernàndez-Cerezo S., Hoyland R. J., Battistelli E. S., 2005, ApJ, 624, L89
Whiteoak J. B. Z., 1994, ApJ, 429, 225
Wilson T. L., Mezger P. G., Gardner F. F., Milne D. K., 1970, A&A, 6, 364

This paper has been typeset from a TEX/LATEX file prepared by the author.